Size-dependent melting of polycyclic aromatic hydrocarbon (PAH) nano-clusters: A molecular dynamics study

Dongping Chen [1], Tim S. Totton [1], Jethro Akroyd [1], Sebastian Mosbach [1],

Markus Kraft [1]

released: 1st July 2013

[1] Department of Chemical Engineering
and Biotechnology
University of Cambridge
New Museums Site
Pembroke Street
Cambridge, CB2 3RA
United Kingdom
E-mail: mk306@cam.ac.uk

Preprint No. 130

UNIVERSITY OF
CAMBRIDGE

Abstract

The size-dependent melting behaviour of clusters of polycyclic aromatic hydrocarbon (PAH) molecules is studied computationally using the isotropic PAHAP potential (Totton *et al.*, 2012, *Physical Chemistry Chemical Physics* **14** 4081–4094). The investigation aims to shed light on the understanding of the liquid-like behaviour of PAH clusters. Detailed molecular dynamic (MD) simulations are performed to investigate the size-dependent melting of two representative homogeneous PAH clusters composed of either pyrene ($C_{16}H_{10}$) or coronene ($C_{24}H_{12}$) molecules. The evolution of the intermolecular energy and the Lindemann Index are used to estimate the melting points of individual nano-clusters. The results from the MD simulations show that individual PAH molecules within nano-clusters are highly mobile below typical flame temperatures. A detailed morphological investigation of coronene$_{500}$ further reveals that the coronene clusters evolve from a columnar particle in the solid phase to an irregular spherical particle in the liquid phase. In contrast, no such evolution is observed for pyrene$_{300}$ which remains in a spherical configuration. A linear decrease in the reduced melting temperature is found with increasing inverse particle size. The melting process of these clusters starts from the surface and the liquid layer grows inwards with increasing temperature.

1

Contents

1 Introduction

Soot morphology has been studied numerically [25, 44, 57] and experimentally [20] for decades but understanding the processes that determine the morphology remains a very challenging and complex problem. Polycyclic aromatic hydrocarbons (PAHs) are often invoked as key precursors to soot formation [10, 40, 41]. This hypothesis assumes soot particles to be comprised of a mixture of PAH molecules, i.e. PAH clusters. However, very little is known about the internal structure and morphology of PAH clusters. Some morphological information can be obtained from high resolution transmission electron microscopy (HR-TEM) images [20] and image analysis techniques can be used to probe the internal particle composition [15, 71].

A number of theoretical studies have also been performed, including investigations of small benzene (C_6H_6) [11, 14, 55, 63, 64, 70], naphthalene ($C_{10}H_8$) [64] and anthracene ($C_{14}H_{10}$) [37] clusters to identify the patterns of the configurations. Rapacioli et al. [44] have investigated assemblies of some larger PAH molecules, from pyrene to circumcoronene, with the cluster sizes ranging from 2 up to 32 molecules. More recently, pyrene and coronene clusters containing up to 50 molecules were investigated theoretically by Totton et al. [57] as analogues of nascent soot particles, with cluster densities calculated using a Monte Carlo integration scheme [39]. In another study, a large ensemble containing 196 irregular PAH molecules (720 Daltons) was investigated via Monte Carlo simulations with atomic pair potentials [25]. Despite the studies of homogenous PAH clusters, very few heterogeneous clusters have been studied in the literature [21]. Most of the bulk PAH compounds, particularly those which are larger than coronene, are not experimentally available. Goddard [18] and coworkers synthesised nearly pure hexabenzocoronene and benzodicoronene crystal samples from pyrene. Unlike usual planar hexabenzocoronene, a novel saddle-shaped molecule was synthesised by embedding a seven-membered ring [28]. The difficulty in the preparation of the bulk system highlights the advantage of computer simulations. In the context of soot inception, the soot community has already benefited from the molecular dynamics method as it allows us to gain the insights of the process form a microscopic point of view [16, 51, 67].

The change in morphology, particularly particle rounding, accounts for the main reduction in surface area of soot particles during the formation and growth of the soot [12]. Consequently, it is extremely important to understand how soot morphology varies in order to improve the predictiveness of current soot models [4, 12, 48]. The melting behaviour of PAH clusters is fundamental to soot morphology. However nano-cluster melting is more complex than that of bulk systems due to finite-size effects and it is generally found that melting temperatures are size-dependent. As the cluster size increases, the melting point approaches that of the bulk system. This is often referred to as melting point depression, and is evident in numerous experimental [5, 9, 49] and theoretical [27, 30, 35, 52, 53] studies. It has been further established that the cluster melting temperature decreases linearly with the reciprocal of cluster diameter [35]. However, a few exceptions exist, such as small sodium clusters which have stable 'magic' icosahedral structures [49].

As discussed by Nanda [34], several different melting mechanisms were proposed to explain the melting behaviour as shown in Figure 1. In the first process, the entire particle is in equilibrium and the melting occurs homogeneously within the entire particle. This
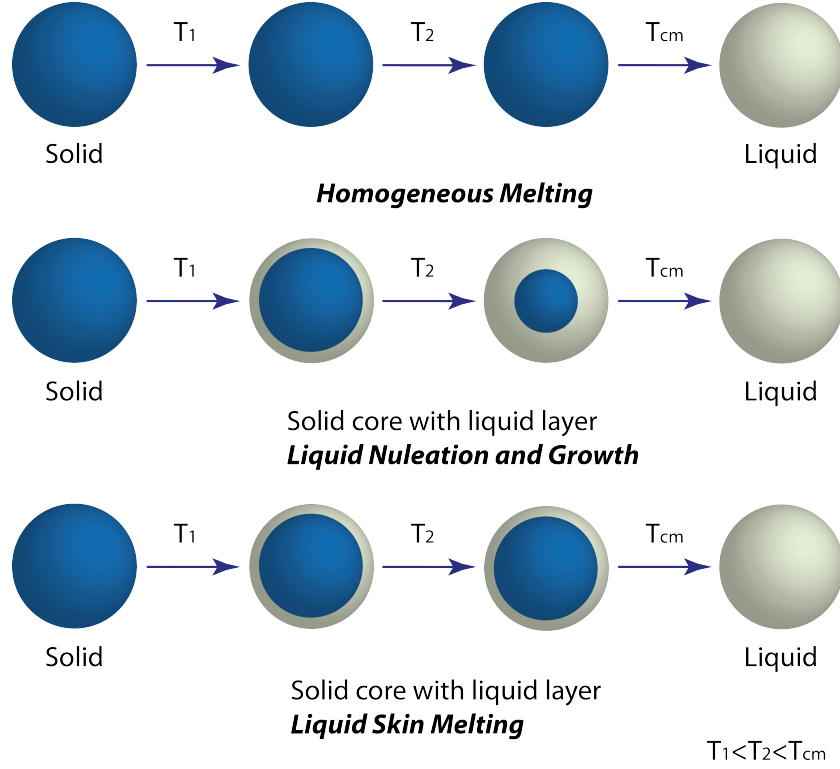
Figure 1: *Three different melting hypotheses for nanoparticles (adapted from [34]).*

mechanism is referred to as the homogeneous melting hypothesis (HMH), with no surface melting observed and the melting temperature T_{cm} of the nanoparticles can be expressed by:

$$\frac{T_{\text{cm}}}{T_{\text{bulk}}} = 1 - \frac{\beta_{HMH}}{D}, \tag{1}$$

where β_{HMH} is a material constant, D is the diameter of the nanoparticle, and T_{bulk} is the bulk melting point. In the second process, which is referred to as liquid nucleation and growth (LNG), a liquid layer forms on the surface and further expands with temperature. Once the liquid layer reaches the core of particle, the particle is completely molten. This mechanism considers that surface melting exists even below melting points and the melting temperature can be given by

$$\frac{T_{\text{cm}}}{T_{\text{bulk}}} = 1 - \frac{\beta_{LNG}}{D}, \tag{2}$$

where β_{LNG} is a material constant.

In the third process, referred to as liquid skin melting (LSM), a liquid layer is formed over the solid core at a low temperature. Unlike the LNG theory, the thickness of the liquid layer remains constant until the entire particle suddenly transforms to liquid at the melting temperature. The expression for the melting temperature is given by

$$\frac{T_{\text{cm}}}{T_{\text{bulk}}} = 1 - \frac{\beta_{LSM}}{D - 2\delta}, \tag{3}$$

4

where β_{LSM} is a material constant, δ is the thickness of the liquid layer.

It may be noted from Eq. 1 and Eq. 2 that both HMH and LNG predict a linear variation of melting temperature with the inverse of size. The only difference between HMH and LNG is the prefactor, β_{HMH} and β_{LNG}. It is obvious from Eq. 3 that LSM predicts a non-linear relationship between the melting temperature and the inverse of the particle size.

In this work, we consider 10 homogenous pyrene and coronene nano-clusters with between 50 and 500 molecules in each cluster. The size-dependent melting behaviour is investigated via conventional molecular dynamics (MD) methods with an isotropic potential for PAH interactions (termed isoPAHAP) developed previously. The melting points of individual nano-clusters are extracted according to the analysis of intermolecular energy, local and global Lindemann index. The morphology evolution is also tracked to investigate the melting process.

2 Computational method

2.1 Intermolecular potential

Recently [62] we have used molecular dynamics simulations of homogeneous PAH systems to determine the size of PAH molecule required for inception of PAH dimers and larger clusters at flame temperatures. The results shed light on the soot inception mechanism and were based on an intermolecular potential fitted to high-level *ab initio* SAPT(DFT) calculations [58, 60, 61]. Originally, we developed this transferable anisotropic potential for PAH molecules (termed PAHAP) considering three types of interaction, C–C, C–H and H–H. However, the PAHAP potential uses angular expansions to take account of the atomic shape anisotropy and such angular dependence is currently not supported by standard MD codes [65]. Consequently, we developed the isoPAHAP potential based on the PAHAP reference potential suitable for use in MD codes [65]. For convenience, we briefly describe the potential here.

Atom-atom intermolecular potentials approximate the total intermolecular interaction energy U as a sum over all pairwise atomic interactions between molecules:

$$U = \sum_A \sum_{A<B} \sum_{a \in A} \sum_{b \in B} U_{ab}(R_{ab}, \Omega_{ab}), \tag{4}$$

where $U_{ab}(R_{ab}, \Omega_{ab})$ denotes an atom-atom interaction potential. The indices A and B are for molecules, and the indices a and b run over all the atomic sites within each molecule. In general the atom-atom interaction potential depends upon the atom-atom separation, R_{ab}, and their relative orientation, denoted generically by Ω_{ab}. However, current MD codes remove the orientational dependence as a simplification assuming that each atom in the molecule has a uniform electron distribution around it.

The form of the isoPAHAP potential is given in Eq. 5 and is identical to the original PAHAP potential except that the shape function ρ is no longer orientation-dependent.

$$U_{ab} = G \exp\left[-\alpha_{ab}(R_{ab} - \rho_{ab})\right] - f_6(R_{ab})\frac{C_{6,\text{iso}}}{R_{ab}^6} + \frac{q_a q_b}{R_{ab}}, \tag{5}$$

5

Table 1: *Parameters for isoPAHAP potential in a.u.^{a}*

atom pair	ρ	α	C_6
C C	6.0434	1.8783	30.282
C H	4.9562	1.7560	12.605
H H	4.1195	1.4043	5.2179

^{a} *The damping coefficient β and the pre-exponential factor G are taken from Ref. 58 to be 1.6485 a.u. and 0.001 a.u. respectively.*

The first term is the short-range Born-Mayer term multiplied by a constant G, set to 0.001 Hartrees, the second is the damped dispersion term and the third is the point-charge electrostatic term. The dispersion is damped with a Tang-Toennies damping function [56] $f_6(R_{ab})$ given by

$$f_n(R_{ab}) = 1 - \exp(-\beta R_{ab}) \sum_{k=0}^{n} \frac{(\beta R_{ab})^k}{k!} \qquad (6)$$

where $\beta = 1.6485$ a.u., taken from Ref [58]. The parameters of isoPAHAP potential were fitted to the interaction energies of 2500 pseudo-random coronene dimer configurations calculated by the PAHAP potential [62]. The resulting parameters for the isoPAHAP potential are shown in Table 1. In order to use this potential in standard MD codes we had to further create a tabulated version including tabulated first derivatives. The step length between the adjacent R_{ab} was set to 0.0005 nm in the tabulated version to ensure the interpolation error is negligible. As discussed in ref [62], PAH molecules are relatively rigid and planar and have limited ability to accommodate kinetic energy into intramolecular modes, making the intermolecular modes the most important for determining PAH cluster stability. However, intramolecular interactions have been accounted for by using the aromatic parameters from the OPLS-AA force field [22, 24] for bonds, angles, dihedrals and improper dihedrals.

2.2 Simulation details

We used conventional MD methods to study the size-dependent melting behaviour of homogenous PAH nano-clusters containing pyrene or coronene molecules (Figure 2). A number of nano-clusters, PAH_N, with N varying from 50 up to 500 (Table 2) were considered. The monomer geometry and atom-centred point-charges for pyrene and coronene molecules were obtained from our previous study [58, 59].

(a)   (b)
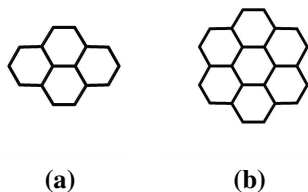
Figure 2: *PAH molecules in this study: (a) Pyrene ($C_{16}H_{10}$), (b) Coronene ($C_{24}H_{12}$).*

For the most part, clusters were simulated at multiple constant temperature conditions

rather than gradually heating and cooling which is the method commonly used in the study of nano-cluster melting. Our method allows us to explore a proper equilibrated configuration at different temperatures and minimise the error introduced by finite equilibration times as shown in Figure 3. The molecules were initially randomly packed within a confined sphere region to create a compact cluster-like configuration by the PACKMOL software package [29]. Minor corrections of the configuration were required to remove abnormally large forces between atoms via an energy minimisation step. This was performed using a two-step minimisation method including a steepest descent algorithm and a quasi-Newtonian algorithm according to the low-memory Broyden-Fletcher-Goldfarb-Shanno approach (L-BFGS) [7]. The simulated annealing (SA) method [26] was then used to produce the initial configurations. Specifically, the clusters were heated to a high temperature state and cooled to a relatively low temperature state in order to allow molecular rearrangement. The entire heating and cooling processes took 1.0 ns. The first 0.4 ns was usually at a constant temperature simulation at low temperature to stabilise the configuration avoiding surface evaporation while heating. For the remaining time, the system was annealed individually only considering the intermolecular interactions with a cut-off of 1.5 nm. The velocity rescaling thermostat [6] was used to control the temperature during the SA step. Specifically, the kinetic energy is rescaled to the target temperature every 0.5 ps.

The final configuration was used as the starting configuration for the determination of the melting point, including at least 8 ns equilibrium (NVT) run and 1 ns production run at a particular temperature. The intermolecular interaction cut-offs of equilibrium and production runs was set to 3.0 nm. The Nosé-Hoover temperature coupling method [19, 36] was used for equilibrium and production runs. This temperature coupling method converges more slowly than the velocity rescaling method but it allows us to probe a correct NVT ensemble. The integration time step was set to 1 fs and trajectories were integrated using the velocity Verlet algorithm [66]. All simulations were performed *in vacuo* without periodic boundary conditions using the Gromacs 4.5.4 program [65]. For each case, the physical quantities (intermolecular energy, Lindemann index, etc.) were averaged within the production run (1 ns trajectory).

2.3   Structure equilibration

To accurately estimate the melting point of individual clusters, a critical step is to probe whether the system is at equilibrium. In other words, the equilibration time is an important consideration when calculating melting points. The equilibration time is defined as the time to equilibrate a particular system at a given temperature. Following the equilibration, physical properties are obtained by further extending the equilibrium run, often referred to as the 'production run'. To investigate how equilibrium time affects our results, we monitored the intermolecular energy evolution of pyrene$_{300}$ and coronene$_{500}$ clusters at 200 K and 550 K respectively (Figure 3) to determine the optimal equilibrium run duration.

In Figure 3b, a systematic drift in the intermolecular energy is observed for coronene$_{500}$. The energy difference between the average of the first 1 ns of the trajectory and that of the last 1 ns is 0.127 eV per number of molecules in the cluster or 0.127 eV/# (approximately

7
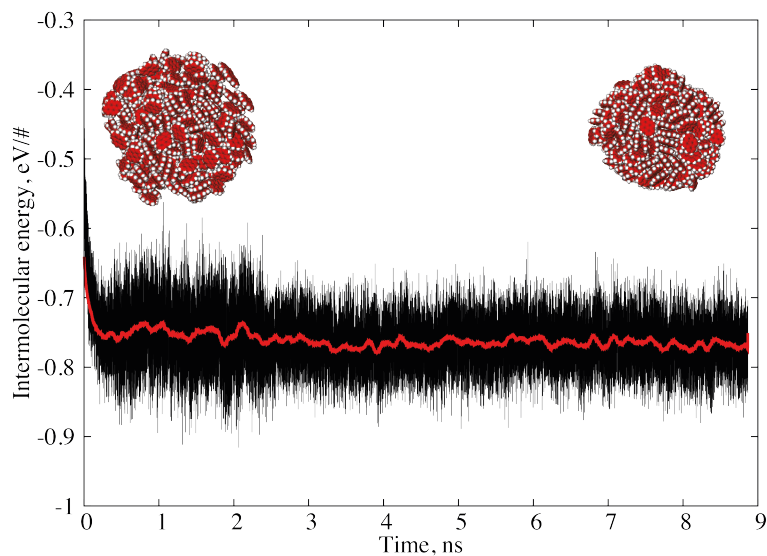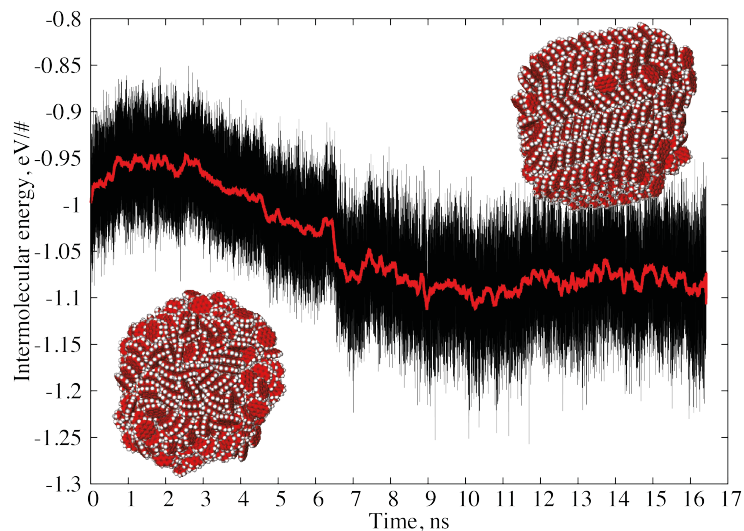
(a) *Pyrene$_{300}$, 200K*

(b) *Coronene$_{500}$, 550K*

Figure 3: *Intermolecular energy evolution of pyrene$_{300}$ and coronene$_{500}$ clusters at 200K and 550K respectively. The red lines represent the evolution of the moving average with 1 ns as window size. The left configurations correspond to the starting configurations at 0 ns for both cases while the right ones correspond to the final configurations of pyrene$_{300}$ at 9 ns and coronene$_{500}$ at 16 ns. The white color represents Hydrogen atom while the red color represents Carbon atom.*

11% of its intermolecular energy). This clear systematic drift starts after approximately 3 ns and ends at 9 ns. During this period, the molecules within coronene$_{500}$ continuously rearrange to a more energetically favourable configuration, i.e. a columnar phase. In contrast, a systematic drift (8%) for pyrene$_{300}$ is only observed within the first 1 ns while the energy drift for the remaining trajectory is small (2%) (Figure 3a).

8

Table 2: *Number of molecules, diameter, inverse diameters and densities of the investigated clusters at their melting points.*

Cluster	Spherical diameter d (nm)	d^{-1} (nm^{-1})	Density (g/cm^{-3})
Pyrene$_{50}$	3.157	0.317	1.02
Pyrene$_{80}$	3.676	0.272	1.03
Pyrene$_{100}$	3.942	0.254	1.05
Pyrene$_{200}$	4.956	0.202	1.05
Pyrene$_{300}$	5.649	0.177	1.07
Coronene$_{50}$	3.518	0.284	1.09
Coronene$_{80}$	4.086	0.245	1.10
Coronene$_{100}$	4.419	0.226	1.10
Coronene$_{200}$	5.529	0.181	1.12
Coronene$_{500}$	7.512	0.133	1.13

Even though the intermolecular energy of pyrene$_{300}$ cluster quickly converged, we select 10 ns as a standard equilibrium setting for all investigated clusters to allow appropriate equilibration of the particle structure.

2.4 Particle properties

The properties of the final configurations of all 10 different sizes pyrene and coronene clusters at their corresponding melting points are summarised in Table 2. The volumes and densities of cluster were calculated according to a Monte Carlo integration routine developed previously [57] and the same calculation parameters were used. The spherical diameters were further calculated by assuming spherical particles.

As shown in Figure 5, the configurations at melting points suggested particles were nearly spherical, and thus we plotted the spherical diameter of individual cluster as a function of $N^{1/3}$ where N is the number of molecules within the cluster (Figure 4). Figure 4 shows a clear linear relationship for pyrene and coronene clusters, and this correlation supports the assumption of spherical particles. However, this correlation may break down at temperatures lower than the melting points when particles may cease to be spherical, e.g. the tube-like configuration of coronene$_{500}$ cluster at 550 K in Fig 10.

2.5 Definition of melting

The melting points of nanoparticles have been determined by monitoring various dynamic and structural properties. The most common criteria used to characterise melting include the Lindemann index [1, 27] (i.e., the root-mean-square bond length fluctuations), radial distribution functions [27, 72] and many different types of caloric curves or heat capacity curves [1]. In the present work, we use intermolecular energy, local (Eq. 9) and global (Eq. 8) Lindemann indices to characterise the solid-liquid transition.

The solid-liquid phase transition temperature is defined as the temperature of the abrupt
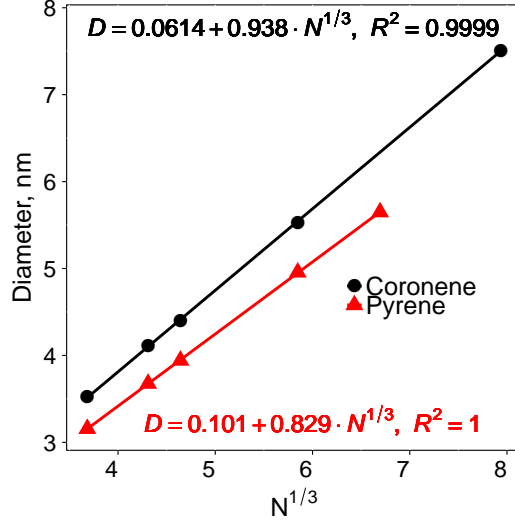
Figure 4: *The spherical diameter of pyrene and coronene clusters as a function of $N^{1/3}$ which N is the number of molecule within a cluster. The equation of the straight lines of best fit and the corresponding R^2 value are shown at the top for coronene cluster and bottom for pyrene cluster respectively.*

change in enthalpy due to the latent heat. The caloric curve is thus expected to jump at the melting point indicating absorption of latent heat and this is the underlying reason that the melting behaviour can be monitored by caloric curves. Furthermore, the molecule in solids undergo small amplitude fluctuations near their equilibrium position, and the fluctuations increase with the temperature. Usually, the Lindemann index which describes root-mean-square (rms) bond fluctuation is used to identify the phase transition temperature. At the melting point, the molecules gain translational freedom and the Lindemann index is increased by as much as a factor of three [27]. The Lindemann index of an individual molecule is expressed as

$$\delta_i = \frac{1}{N-1} \sum_{j \neq i} \frac{\sqrt{\langle r_{ij}^2 \rangle_T - \langle r_{ij} \rangle_T^2}}{\langle r_{ij} \rangle_T}, \tag{7}$$

where i and j are the index of ith and jth molecule, respectively, δ_i is Lindemann index of the ith molecule, $\langle \ldots \rangle_T$ represents an average quantity over 1 ns at temperature T, r_{ij} is the distance between centre of mass of molecule i and that of molecule j.

The global Lindemann index is expressed as

$$\delta_G = \frac{1}{N} \sum_{i \in N} \delta_i, \tag{8}$$

where δ_G is global Lindemann index of cluster, and N is the number of molecules within the individual cluster.

To explicitly investigate the local melting phenomenon, the cluster was divided into concentric shells with the same thickness (3.5 Å) which is the layer separation of PAH
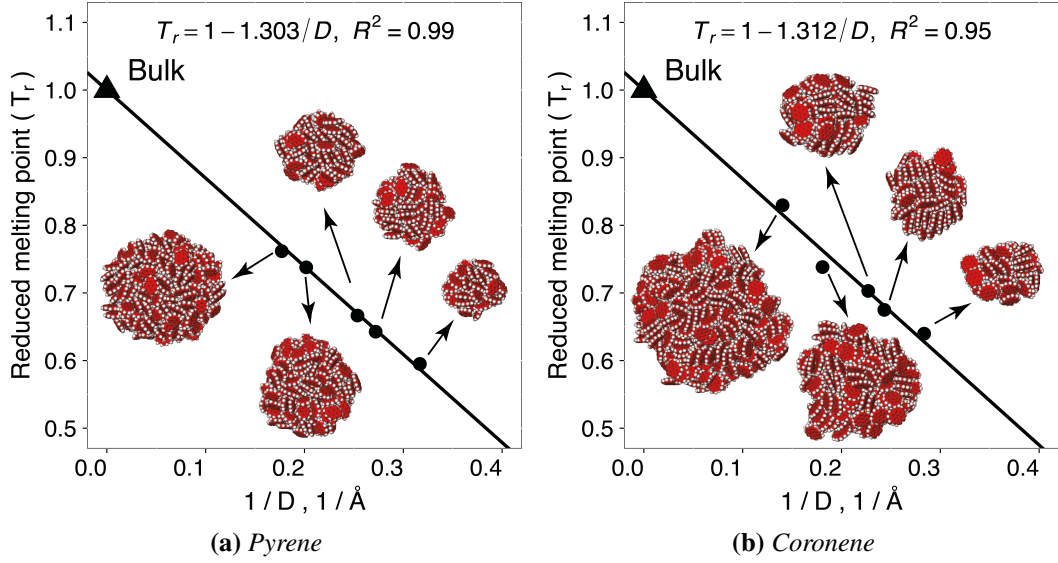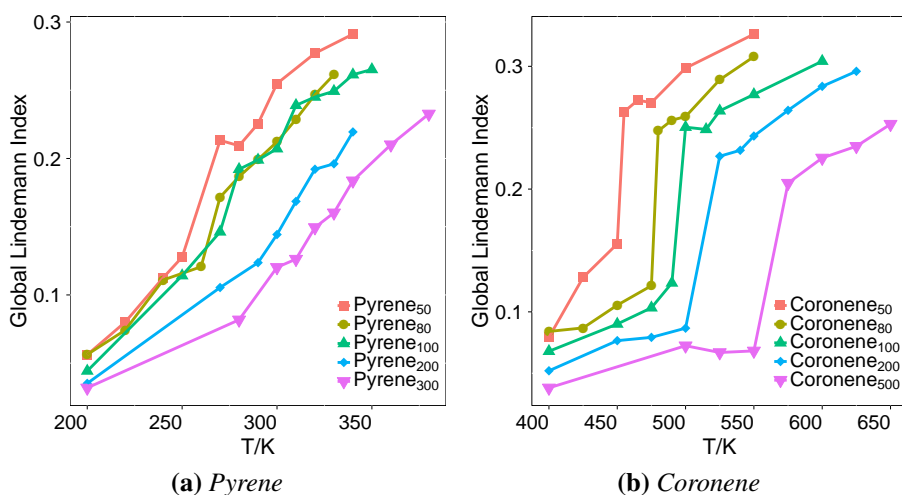
(a) *Pyrene*   **(b)** *Coronene*

Figure 5: *The reduced melting temperature as a function of inverse diameter for the pyrene and coronene clusters. T_r is the reduced melting point of individual cluster (T_{cm}/T_{bulk}). The triangles, ▲, indicate experimentally measured bulk melting points. T_{bulk} of pyrene and coronene is 424.3 K [23] and 710.5 K [54] respectively. The configurations of each size clusters at their corresponding melting point are also embedded on the plot with the relative sizes of the clusters preserved. Also included are details about the fitted curves.*

stacks [33, 57]. Molecules can then be assigned to each shell according to the distance to the mass centre of the final configuration.

Let S represent a set containing the molecule indices in a particular shell. The local Lindemann index of each shell is defined as

$$\delta_L = \frac{1}{|S|} \sum_{i \in S} \delta_i,$$
(9)

where δ_L is local Lindemann index of each shell, $|S|$ represents the number of molecules in the corresponding shell. One benefit of using δ_L is that we can individually monitor the local mobility of each shell, i.e. surface-melting phenomena can be directly observed if they exist. Furthermore, the melting point of the individual cluster can be estimated by analysing δ_L. Clusters melt at the temperature at which δ_L near the cluster core shows no obvious difference compared to that at the surface.

11

Figure 6: *Global Lindemann Index of pyrene and coronene clusters.*
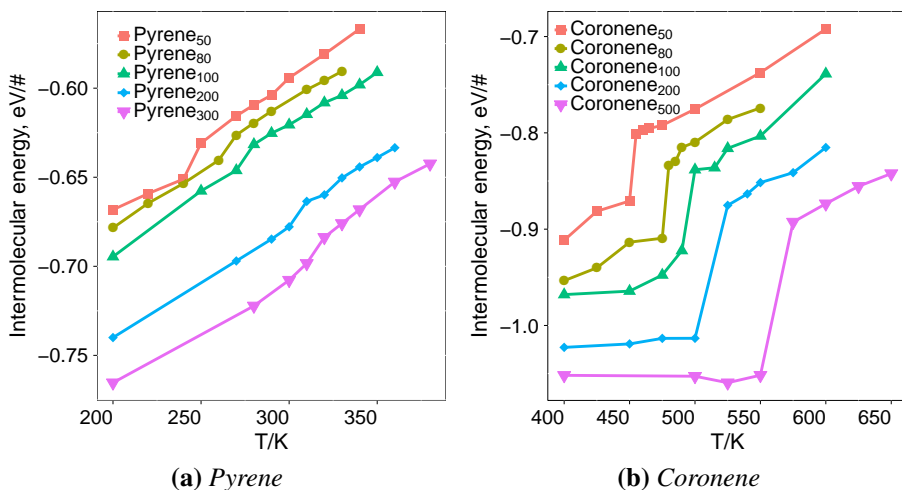
Figure 7: *Average intermolecular energy per molecule as a function of temperature for different size pyrene and coronene clusters. The size of the clusters ranges from 50–500 molecules per cluster.*

3 Results and discussion

3.1 Cluster melting temperatures

All three melting monitoring methods were applied to all the clusters, and the reduced melting points obtained are plotted in Figure 5 as a function of inverse diameter. The reduced melting point is defined as the melting point of individual cluster divided by that of bulk system. From Figure 5, it is clear that the predicted melting points yield a linear dependence on the inverse diameter of the clusters which is observed in experiments and numerical studies for metal atom systems [35]. The labelled 'bulk' point indicates the

**Table 3:** *Melting points and energy jump of the investigated clusters.*

Cluster	Melting point (K)	Energy jump (eV/#)
Pyrene$_{50}$	250	0.0121
Pyrene$_{80}$	270	0.0068
Pyrene$_{100}$	280	0.0146
Pyrene$_{200}$	310	0.0143
Pyrene$_{300}$	320	0.0147
Coronene$_{50}$	455	0.070
Coronene$_{80}$	480	0.094
Coronene$_{100}$	500	0.084
Coronene$_{200}$	525	0.138
Coronene$_{500}$	575	0.159

bulk melting point from experiments (corresponding to $D \to \infty$). The melting points and energy jumps due to melting of individual clusters are given in Table 3. Unsurprisingly, the size of the energy jumps increase with the size of cluster and this indicates that higher energy is required to melt clusters with more molecules. Rapacioli et al. [45] predicted the melting point of coronene$_8$ was 200 K using Monte Carlo simulation with the all-exchange parallel tempering strategy [8]. This method allows an efficient approach to the global minimum of the intermolecular energy. To interpret their caloric curve, they treated peaks in the classical heat capacity as the signature of the melting phase change that is associated with the thermal instability of the molecular stack sub-configurations. By comparison, we predicted the melting point of coronene$_8$ to be 219 K by linear extrapolation of curve shown in Figure 5b. The spherical diameter of coronene$_8$ is 1.936 nm and was computed according to the linear relationship found between the spherical diameter of the individual cluster and $N^{1/3}$, where N is the number of molecules within a cluster, as shown in Figure 4.

Figure 6 and Figure 7 show the global Lindemann index and intermolecular energy per molecule for particles of various sizes against the temperatures for pyrene and coronene clusters respectively. The global Lindemann index of coronene clusters abruptly increased as suggested from the local Lindemann index curves (Figure 8), and a similar significant increase in the intermolecular energy was also be seen at the same temperature. Hence, this temperature is interpreted as the melting point of individual clusters (Table 3). However, no such abrupt changes are seen for the pyrene clusters. Instead, the global Lindemann index gradually increases with the temperature for all clusters, and similarly, there are no noticeable jumps in the intermolecular energy.

3.2 Mode of particle melting

The solid-liquid transition was also monitored by the local Lindemann index as a function of distance to the centre of mass of the cluster, as shown in Figures 8 and 9 for coronene and pyrene clusters, respectively. Different size coronene clusters under four typical temperatures have been used to investigate the mobility of molecules within an individual

(a) *Coronene*$_{50}$

(b) *Coronene*$_{80}$

(c) *Coronene*$_{100}$

(d) *Coronene*$_{200}$

(e) *Coronene*$_{500}$
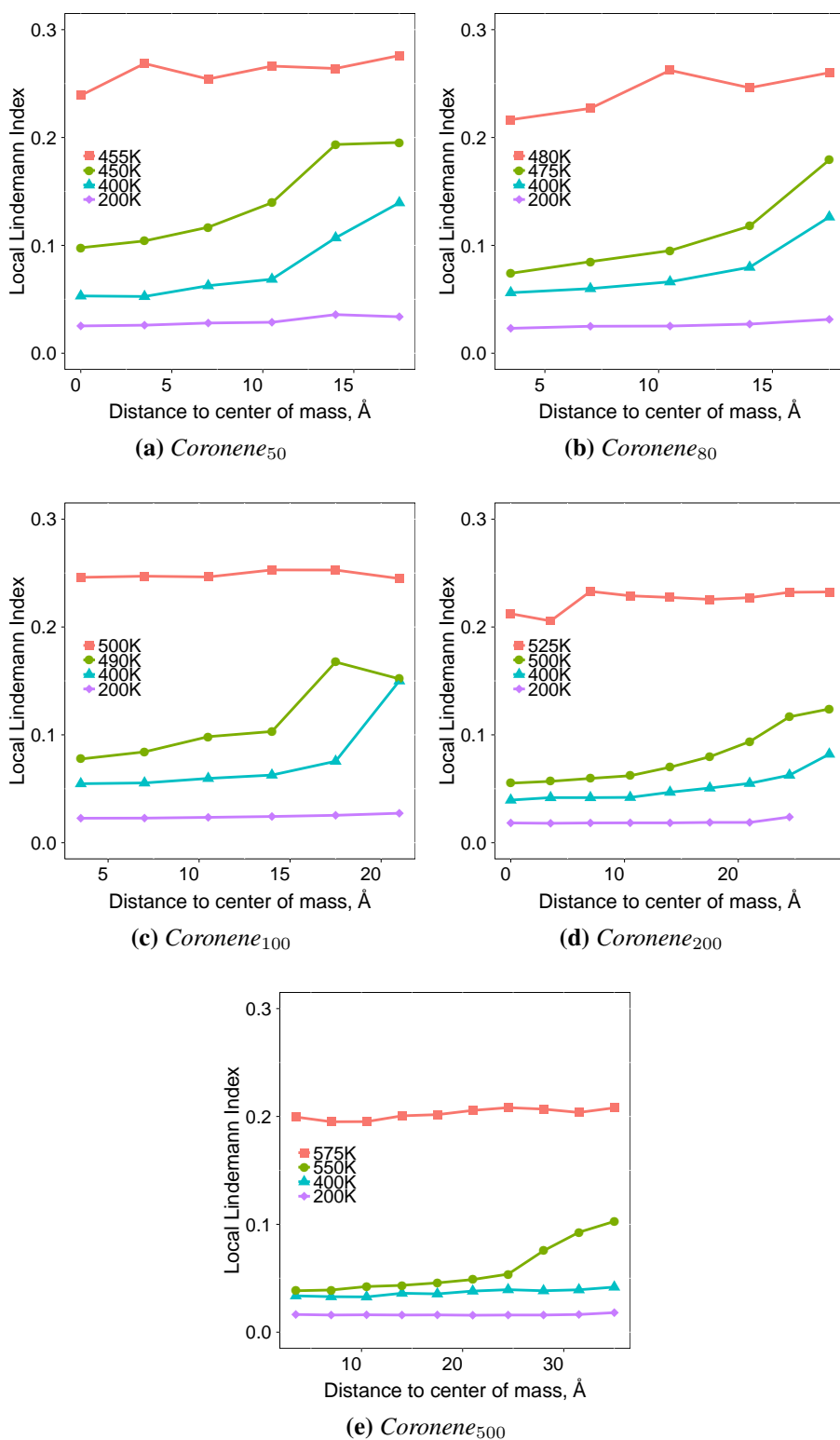
Figure 8: *Radial distribution of local Lindemann Index of coronene clusters, the size of the clusters ranges from 50–500 coronene molecules per cluster.*
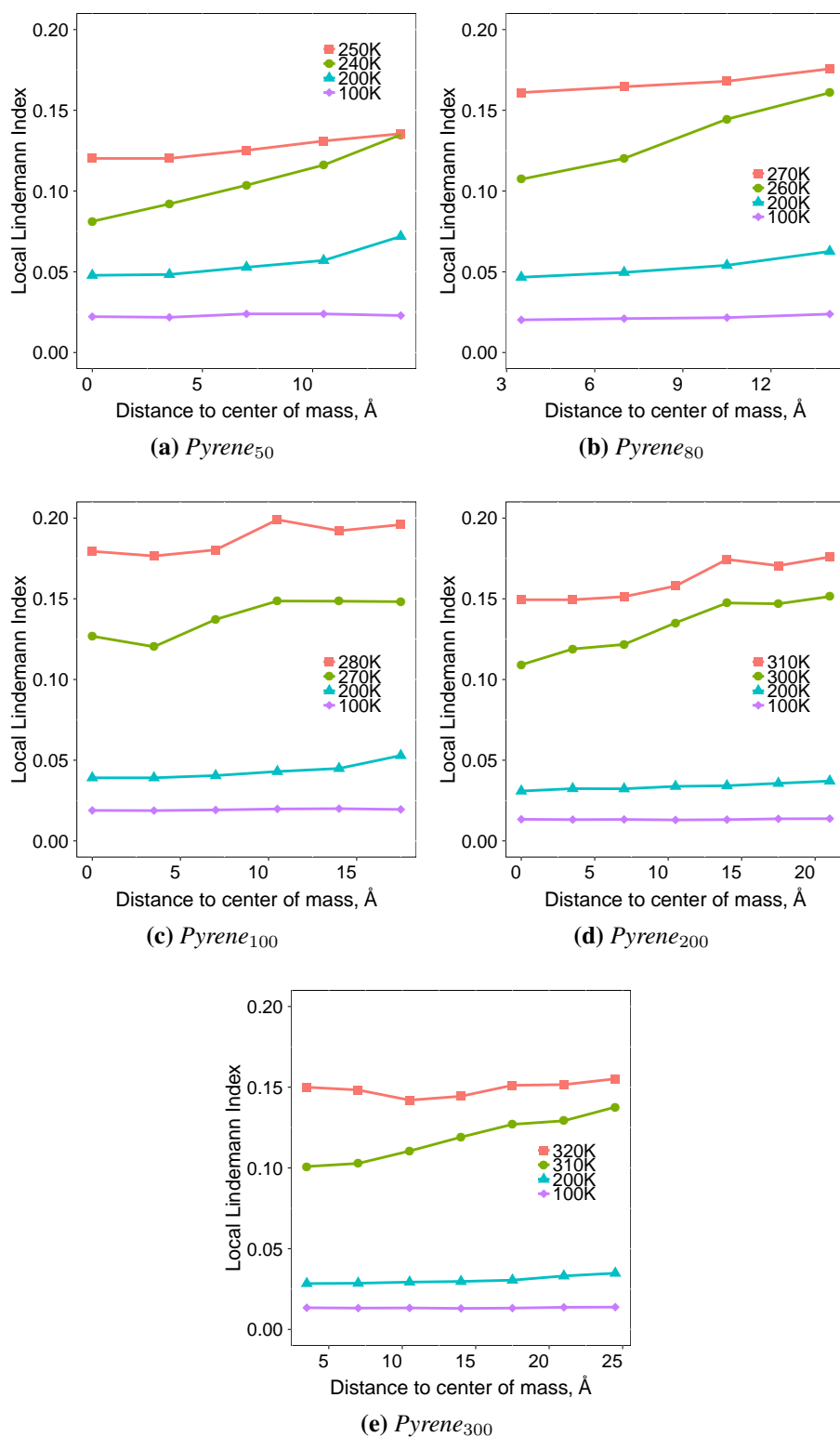
**Figure 9:** *Radial distribution of local Lindemann Index of pyrene clusters, the size of the clusters ranges from 50–300 pyrene molecules per cluster.*

cluster. At the lowest temperature, i.e. 200 K which is far below the melting point, the local Lindemann index of all the cases is less than 0.05 and no difference is observed between the cluster centre and the surface. This observation suggests that the nanoparticle is in the solid phase, and this is unsurprising since molecular fluctuations are limited at such low temperatures. When increasing the temperature to 400 K, the clusters show size-dependent behaviour. For the small clusters, i.e. coronene$_{50}$, coronene$_{80}$ and coronene$_{100}$, the local Lindemann indices at the surface are approximately two times higher than those near the cluster centre. This indicates that molecules at the surface have greater freedom while molecules at the cluster centre have less freedom to vibrate due to the stronger interactions around them. In other words, this phenomenon can be interpreted as surface melting [53]. However, this variation in mobility between surface and core decreases as the cluster size increases. For coronene$_{500}$, no such difference can be observed, and the local Lindemann index remains constant across the cluster. For cases where the temperature is slightly lower than the cluster melting point, surface melting is clear for all cases. At the melting point, the local Lindemann curves of all the coronene cases become flat indicating that the mobility of molecules at the core and at the surface are nearly the same. Furthermore, the higher values, which are approximately three times greater than that at temperatures slightly lower than their melting points, indicate that all the molecules within each respective cluster gain translational freedom and consequently, the cluster is in the liquid state. In summary, it can be concluded that, for coronene clusters, surface melting is a common pre-melting behaviour at temperatures sightly below the melting point.

For pyrene clusters (Figure 9), the local Lindemann index behaves differently compared to coronene clusters, particularly at temperature close to the melting point. At 100 K, the local Lindemann index of all cases remains very small due to such low temperatures and when increasing the temperature to 200 K, no size-dependent behaviour is found. When further increasing the temperature to a value close to the melting point, the mobility of molecules at the cluster centre is high and the difference between the mobility of core and surface molecules is much lower than found with the coronene clusters. However, molecules at the surface are more diffusive than the core molecules. We speculate that the formation of big stacked configurations, coronene$_{500}$ at 550 K shown in Figure 10, limit the fluctuation of molecules at the cluster centre, and result in a reduced local Lindemann index. However, such configurations are not readily observed in the pyrene clusters allowing core molecules to move more freely and resulting in no significant variation between the local Lindemann index of the surface shell compared to that of the centre shell, at temperatures sightly lower than the melting point. Again, with further heating the local Lindemann index curve becomes flat indicating complete melting.

It is concluded that the mode of coronene cluster melting follows the LNG theory as shown on Fig 1. The clear surface melting phenomenon is observed at temperatures lower than the melting point and this suggest a formation of liquid skin. As increasing the temperature, for instance, the coronene$_{100}$, the liquid skin expands from the first shell at 400 K to the second shell at 490K. In contrast, the melting behaviour of pyrene clusters seems to be intermediate between the homogenous melting and liquid nucleation and growth mechanisms.

16
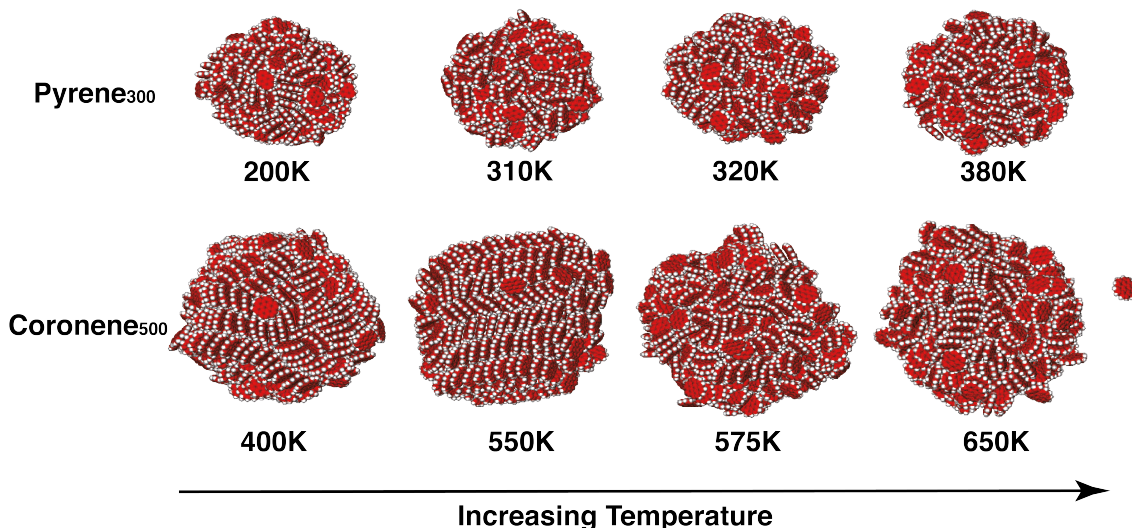
Figure 10: *Morphology evolution of coronene$_{500}$ and pyrene$_{300}$ from solid to liquid.*

3.3 Morphology of pyrene and coronene clusters

To further investigate the melting behaviour, the evolution of the particle morphology was examined visually for the largest pyrene and coronene clusters, pyrene$_{300}$ and coronene$_{500}$. In Figure 10, configurations of coronene$_{500}$ and pyrene$_{300}$ at four representative temperatures are shown; 400 K and 200 K represents a solid phase far below the melting point of each cluster, 550 K and 310 K represents a solid phase slightly below the melting points, 575 K and 320 K represents a liquid phase slightly above the melting points and 650 K and 380 K represents a liquid phase far above the melting points, respectively.

At 400 K, coronene$_{500}$ is a combination of different size stacks in which the largest one contains 12 coronene molecules while the smallest contains 3 molecules. From a thermodynamical point of view, the temperature is so low that the configuration is effectively trapped in this local minimum configuration. It is unlikely that the cluster can overcome the energy barriers associated with moving out of this local minimum without further heating. In contrast, at 550 K coronene$_{500}$ forms a columnar particle containing multiple long parallel stacks. It is worth noting that the prediction of such a configuration is strongly dependent on allowing the system a sufficiently long time to equilibrate (see Figure 3b). This packing behaviour is referred to as a columnar phase, or discotic configuration [2]. This type of packing has been seen experimentally with x-ray diffraction experiments [17] for derivatives of hexabenzocoronene ($C_{48}H_{18}$) clusters at room temperature. These results suggest that the equilibrated structures of large planar PAH molecules should form a columnar phase, as found here. Furthermore, Rapacioli et al. [43] also found the columnar phase for a coronene$_{32}$ cluster as the global minimum configuration.

At 575 K, the configuration of coronene$_{500}$ becomes a cluster composed of smaller stacks again. However, the underlying reason is different from 400 K case. Now as a liquid, the higher kinetic energy of individual molecules destabilises the columnar stack configuration resulting in the formation of small stacks, each with fewer than 10 molecules.

At 650 K, the configuration is very similar to 575 K case, however, a molecule on the

right has evaporated from the surface. In total seven molecules moved away from the surface during the first 3 ns of the simulation. In fact, single molecule evaporation was first noticed at 525 K. This is in line with experimental findings which indicate molecules begin to evaporate from coronene clusters at 535 ± 50 K [50].

Unlike coronene$_{500}$, the configuration of pyrene$_{300}$ does not form a columnar phase. The stacking interaction between pyrene molecules is not as strong as that seen with coronene molecules due to reduced π–π interactions [62] and a higher proportion of hydrogen atoms, which both contribute to greater instability in large pyrene stacks such that they are not energetically favourable configurations.

This study has focused on the melting behaviour of pericondensed aromatic hydrocarbons (PCAH). It is concluded that the clusters begin to have liquid-like properties when individual molecules obtain sufficiently high kinetic energy to perform large-amplitude motion at high temperatures. The mobility of individual PAH molecules is enhanced further by the increase of the temperature. This observation suggests the feasibility of sintering process between neighbour primary particles within a coronene or pyrene aggregate. Such process is driven by molecular diffusion and accounts for particle rounding due to the rearrangement of molecules without any change in the mass of an aggregate [12]. Furthermore, the investigated clusters in this study (Table 2) have very similar physical properties to nascent soot particles [13], such as the size and material density. The results in this present work therefore shed light on the transition of nascent soot particles from coalescence or fully sintered to fractal growth. This transition is not well understood in the soot community. It is believed that at small sizes particles are liquid-like leading to complete coalescence. However, larger particles are only partially coalesced due to transient nature of soot formation which provides insufficient time to allow full particle rounding [38]. In an alternative view, particle rounding and further evolution and growth to fractal structures occurs predominantly by surface growth and particle aggregation [3, 31, 32, 69].

The results of the present work suggests that we observed liquid-like nanoparticles of homogenous pyrene and coronene molecules even below 600 K. This observation indicates the existence of liquid-like soot particles at flame temperatures (1500-2000 K), or at least a liquid shell on the particle surface [68]. Recent research indicates that clusters composed of small PAH molecules, such as pyrene and coronene, are unlikely to be stable at flame temperatures [42, 46, 62]. However, it has been recently argued that enhanced interactions, i.e. between localised molecular charges, may allow for stable binding between smaller PAH molecules [68], although this is yet to be confirmed.

Even if pyrene and coronene clusters are not stable in flame conditions, the present observations suggest larger PCAH molecules e.g. circumcoronene ($C_{54}H_{18}$), may well be highly mobile within particles in this environment. This would allow particle rounding by sintering, although the extent of morphological change will depend on the composition and the residence time in the flame. This is in line with our previous work [12, 47] in which a population balance model was fitted to measured particles size distribution. It was found that sintering played a very important role in forming soot aggregates. In the light of the results of our MD study this rounding mechanism is plausible.

4   Conclusions

Molecular dynamic simulations using a previously developed PAH intermolecular potential were performed to study the size dependent melting behaviour of pyrene and coronene clusters with diameters from 3 to 8 nm, which are typical of the size of nascent soot particles. The melting process was followed by monitoring the local and global Lindemann indexes for the clusters, as well as the caloric curves and visual inspection of the cluster morphology evolution. A linear decrease in the reduced melting temperature was found with increasing inverse particle size. Surface melting was also suggested from local Lindemann index analysis. Coronene clusters were found to form a distinct columnar phase as a solid which was then disrupted upon melting such that only small stacks were observed in the liquid phase. It was also found that the evaporation of coronene molecules occurred near to the melting point. However, the pyrene clusters did not show any preference for the columnar phase, even at low temperature (200 K), due to its reduced π-bonding interaction and higher hydrogen proportion. Instead, the pyrene clusters only contained small stacks of up to 9 molecules. The present results show that individual PAH molecules within nascent soot particles are likely to be highly mobile at flame temperatures. This suggests that sintering between soot particles in the flame environment is likely, particularly for small particles with diameters less than 10 nm.

5   Acknowledgements

References

[1] S. Alavi and D. L. Thompson. Molecular dynamics simulations of the melting of aluminum nanoparticles. *The Journal of Physical Chemistry A*, 110(4):1518–1523, 2006. doi:10.1021/jp053318s.

[2] D. Andrienko, V. Marcon, and K. Kremer. Atomistic simulation of structure and dynamics of columnar phases of hexabenzocoronene derivatives. *The Journal of Chemical Physics*, 125(12):124902, 2006. doi:10.1063/1.2354156.

[3] M. Balthasar and M. Frenklach. Detailed kinetic modeling of soot aggregate formation in laminar premixed flames. *Combustion and Flame*, 140:130–145, 2005. doi:10.1016/j.combustflame.2004.11.004.

[4] M. Balthasar, F. Mauss, A. Knobel, and M. Kraft. Detailed modeling of soot formation in a partially stirred plug flow reactor. *Combustion and Flame*, 128(4):395 – 409, 2002. doi:10.1016/S0010-2180(01)00344-3.

[5] P. Buffat and J.-P. Borel. Size effect on the melting temperature of gold particles. *Physical Review A*, 13:2287–2298, 1976. doi:10.1103/PhysRevA.13.2287.

[6] G. Bussi, D. Donadio, and M. Parrinello. Canonical sampling through velocity rescaling. *The Journal of Chemical Physics*, 126(1):014101, 2007. doi:10.1063/1.2408420.

[7] R. Byrd, P. Lu, J. Nocedal, and C. Zhu. A limited memory algorithm for bound constrained optimization. *SIAM Journal on Scientific Computing*, 16(5):1190–1208, 1995. doi:10.1137/0916069.

[8] F. Calvo. All-exchanges parallel tempering. *The Journal of Chemical Physics*, 123 (12):124106, 2005. doi:10.1063/1.2036969.

[9] T. Castro, R. Reifenberger, E. Choi, and R. P. Andres. Size-dependent melting temperature of individual nanometer-sized metallic clusters. *Physical Review B*, 42: 8548–8556, 1990. doi:10.1103/PhysRevB.42.8548.

[10] M. Celnik, A. Raj, R. West, R. Patterson, and M. Kraft. Aromatic site description of soot particles. *Combustion and Flame*, 155(1):161 – 180, 2008. doi:10.1016/j.combustflame.2008.04.011.

[11] D. Chakrabarti, T. S. Totton, M. Kraft, and D. Wales. A survey of the potential energy surface for (benzene)$_{13}$ cluster. *Physical Chemistry Chemical Physics*, 13 (48):21362–21366, 2011. doi:10.1039/C1CP22220A.

[12] D. Chen, Z. Zainuddin, E. Yapp, J. Akroyd, S. Mosbach, and M. Kraft. A fully coupled simulation of PAH and soot growth with a population balance model. *Proceedings of the Combustion Institute*, 34(1):1827 – 1835, 2013. doi:10.1016/j.proci.2012.06.089.

[13] R. A. Dobbins. Hydrocarbon nanoparticles formed in flames and diesel engines. *Aerosol Science and Technology*, 41(5):485–496, 2007. doi:10.1080/02786820701225820.

[14] D. C. Easter. Identification of a new C_3 structure and evidence for the co-existence of two (Benzene)$_{13}$ cluster isomers in free jet expansions: A Monte Carlo study. *The Journal of Physical Chemistry A*, 107(39):7733–7742, 2003. doi:10.1021/jp035694n.

[15] V. Fernandez-Alos, J. K. Watson, R. Vander Wal, and J. P. Mathews. Soot and char molecular representations generated directly from HRTEM lattice fringe images using Fringe3D. *Combustion and Flame*, 158(9):1807–1813, 2011. doi:10.1016/j.combustflame.2011.01.003.

[16] S. L. Fiedler, S. Izvekov, and A. Violi. The effect of temperature on nanoparticle clustering. *Carbon*, 45(9):1786–1794, 2007. doi:10.1016/j.carbon.2007.05.001.

[17] I. Fischbach, T. Pakula, P. Minkin, A. Fechtenkötter, K. Müllen, H. W. Spiess, and K. Saalwächter. Structure and dynamics in columnar discotic materials: A combined X-ray and solid-state NMR study of hexabenzocoronene derivatives. *The Journal of Physical Chemistry B*, 106(25):6408–6418, 2002. doi:10.1021/jp0255684.

[18] R. Goddard, M. W. Haenel, W. C. Herndon, C. Krueger, and M. Zander. Crystallization of large planar polycyclic aromatic hydrocarbons: The molecular and crystal structures of hexabenzo[bc,ef,hi,kl,no,qr]coronene and benzo[1,2,3-bc:4,5,6-b'c']dicoronene. *Journal of the American Chemical Society*, 117(1):30–41, 1995. doi:10.1021/ja00106a004.

[19] W. G. Hoover. Canonical dynamics: Equilibrium phase-space distributions. *Physical Review A*, 31(3):1695–1697, 1985. doi:10.1103/PhysRevA.31.1695.

[20] T. Ishiguro, Y. Takatori, and K. Akihama. Microstructure of diesel soot particles probed by electron microscopy: First observation of inner core and outer shell. *Combustion and Flame*, 108:231–234, 1997. doi:10.1016/S0010-2180(96)00206-4.

[21] W. L. Jorgensen and D. L. Severance. Aromatic-aromatic interactions: free energy profiles for the benzene dimer in water, chloroform, and liquid benzene. *Journal of the American Chemical Society*, 112(12):4768–4774, 1990. doi:10.1021/ja00168a022.

[22] W. L. Jorgensen, D. S. Maxwell, and J. Tirado-Rives. Development and testing of the OPLS all-atom force field on conformational energetics and properties of organic liquids. *Journal of the American Chemical Society*, 118(45):11225–11236, 1996. doi:10.1021/ja9621760.

[23] C. L. Judy, N. M. Pontikos, and W. E. Acree. Solubility of pyrene in binary solvent mixtures containing cyclohexane. *Journal of Chemical & Engineering Data*, 32(1): 60–62, 1987. doi:10.1021/je00047a018.

[24] G. A. Kaminski, R. A. Friesner, J. Tirado-Rives, and W. L. Jorgensen. Evaluation and reparametrization of the OPLS-AA force field for proteins via comparison with accurate quantum chemical calculations on peptides. *The Journal of Physical Chemistry B*, 105(28):6474–6487, 2001. doi:10.1021/jp003919d.

[25] R. Khanna, V. Sahajwalla, and R. H. Hurt. An atomistic technique for simulating non-covalent interactions in large ensembles of high-molecular-weight polyaromatics. *Carbon*, 43(1):67–77, 2005. doi:10.1016/j.carbon.2004.08.023.

[26] S. Kirkpatrick, C. D. Gelatt, and M. P. Vecchi. Optimization by simulated annealing. *Science*, 220(4598):671–680, 1983. doi:10.1126/science.220.4598.671.

[27] V. N. Koparde and P. T. Cummings. Sintering of titanium dioxide nanoparticles: A comparison between molecular dynamics and phenomenological modeling. *Journal of Nanoparticle Research*, 10(7):1169–1182, 2008. doi:10.1007/s11051-007-9342-3.

[28] J. Luo, X. Xu, R. Mao, and Q. Miao. Curved polycyclic aromatic molecules that are p-isoelectronic to hexabenzocoronene. *Journal of the American Chemical Society*, 134(33):13796–13803, 2012. doi:10.1021/ja3054354.

[29] L. Martínez, R. Andrade, E. G. Birgin, and J. M. Martínez. Packmol: A package for building initial configurations for molecular dynamics simulations. *Journal of Computational Chemistry*, 30(13):2157–2164, 2009. doi:10.1002/jcc.21224.

[30] Q. Mei and K. Lu. Melting and superheating of crystalline solids: From bulk to nanocrystals. *Progress in Materials Science*, 52(8):1175 – 1262, 2007. doi:10.1016/j.pmatsci.2007.01.001.

[31] P. Mitchell and M. Frenklach. Particle aggregation with simultaneous surface growth. *Physical Review E*, 67:061407, 2003. doi:10.1103/PhysRevE.67.061407.

[32] N. Morgan, M. Kraft, M. Balthasar, D. Wong, M. Frenklach, and P. Mitchell. Numerical simulations of soot aggregation in premixed laminar flames. *Proceedings of the Combustion Institute*, 31(1):693–700, 2007. doi:10.1016/j.proci.2006.08.021.

[33] S. Mosbach, M. S. Celnik, A. Raj, M. Kraft, H. R. Zhang, S. Kubo, and K. Kim. Towards a detailed soot model for internal combustion engines. *Combustion and Flame*, 156(6):1156–1165, 2009. doi:10.1016/j.combustflame.2009.01.003.

[34] K. K. Nanda. Size-dependent melting of nanoparticles: Hundred years of thermodynamic model. *Pramana*, 72(4):617–628, 2009. doi:10.1007/s12043-009-0055-2.

[35] E. C. Neyts and A. Bogaerts. Numerical study of the size-dependent melting mechanisms of Nickel nanoclusters. *The Journal of Physical Chemistry C*, 113(7):2771–2776, 2009. doi:10.1021/jp8058992.

[36] S. Nosé. A unified formulation of the constant temperature molecular dynamics methods. *The Journal of Chemical Physics*, 81(1):511–519, 1984. doi:10.1063/1.447334.

[37] F. Piuzzi, I. Dimicoli, M. Mons, P. Millié, V. Brenner, Q. Zhao, B. Soep, and A. Tramer. Spectroscopy, dynamics and structures of jet formed anthracene clusters. *Chemical Physics*, 275(1 - 3):123 – 147, 2002. doi:10.1016/S0301-0104(01)00534-1.

[38] G. Prado, J. Jagoda, K. Neoh, and J. Lahaye. A study of soot formation in premixed propane/oxygen flames by in-situ optical techniques and sampling probes. *Symposium (International) on Combustion*, 18(1):1127 – 1136, 1981. doi:10.1016/S0082-0784(81)80117-8.

[39] W. H. Press, S. A. Teukolsky, W. T. Vetterling, and B. P. Flannery. *Numerical Recipes in C++ The Art of Scientific Computing*. Cambridge University Press, Cambridge, 2nd edition, 2002.

[40] A. Raj, M. Celnik, R. Shirley, M. Sander, R. Patterson, R. West, and M. Kraft. A statistical approach to develop a detailed soot growth model using PAH characteristics. *Combustion and Flame*, 156(4):896 – 913, 2009. doi:10.1016/j.combustflame.2009.01.005.

[41] A. Raj, P. L. Man, T. S. Totton, M. Sander, R. A. Shirley, and M. Kraft. New polycyclic aromatic hydrocarbon (PAH) surface processes to improve the model prediction of the composition of combustion-generated PAHs and soot. *Carbon*, 48 (2):319 – 332, 2010. doi:10.1016/j.carbon.2009.09.030.

[42] A. Raj, M. Sander, V. Janardhanan, and M. Kraft. A study on the coagulation of polycyclic aromatic hydrocarbon clusters to determine their collision efficiency. *Combustion and Flame*, 157(3):523 – 534, 2010. doi:10.1016/j.combustflame.2009.10.003.

[43] M. Rapacioli, F. Calvo, F. Spiegelman, C. Joblin, and D. J. Wales. Stacked clusters of polycyclic aromatic hydrocarbon molecules. *Journal of Physical Chemistry A*, 109(11):2487–2497, 2005. doi:10.1021/jp046745z.

[44] M. Rapacioli, F. Calvo, F. Spiegelman, C. Joblin, and D. J. Wales. Stacked clusters of polycyclic aromatic hydrocarbon molecules. *Jounal of Physical Chemistry A*, 109:2487–2497, 2005. doi:10.1021/jp046745z.

[45] M. Rapacioli, F. Calvo, C. Joblin, P. Parneix, and F. Spiegelman. Vibrations and thermodynamics of clusters of polycyclic aromatic hydrocarbon molecules: The role of internal modes. *The Journal of Physical Chemistry A*, 111(16):2999–3009, 2007. doi:10.1021/jp068821z.

[46] H. Sabbah, L. Biennier, S. J. Klippenstein, I. R. Sims, and B. R. Rowe. Exploring the role of PAHs in the formation of soot: Pyrene dimerization. *The Journal of Physical Chemistry Letters*, 1(19):2962–2967, 2010. doi:10.1021/jz101033t.

[47] M. Sander, R. H. West, M. S. Celnik, and M. Kraft. A detailed model for the sintering of polydispersed nanoparticle agglomerates. *Aerosol Science and Technology*, 43 (10):978–989, 2009. doi:10.1080/02786820903092416.

[48] M. Sander, R. I. Patterson, A. Braumann, A. Raj, and M. Kraft. Developing the PAH-PP soot particle model using process informatics and uncertainty propagation. *Proceedings of the Combustion Institute*, 33(1):675 – 683, 2011. doi:10.1016/j.proci.2010.06.156.

[49] M. Schmidt, R. Kusche, and H. Haberland. Irregular variations in the melting point of size-selected atomic clusters. *Nature*, 393(6682):238–240, 1998. doi:10.1038/30415.

[50] M. Schmidt, A. Masson, and C. Bréchignac. Coronene cluster experiments: Stability and thermodynamics. *International Journal of Mass Spectrometry*, 252(2):173–179, 2006. doi:10.1016/j.ijms.2005.10.015.

[51] C. A. Schuetz and M. Frenklach. Nucleation of soot: Molecular dynamics simulations of pyrene dimerization. *Proceedings of the Combustion Institue*, 29:2307–2314, 2002.

[52] Y. Shibuta and T. Suzuki. A molecular dynamics study of the phase transition in bcc metal nanoparticles. *The Journal of chemical physics*, 129(14):144102, 2008. doi:10.1063/1.2991435.

[53] Q. Shu, Y. Yang, Y. T. Zhai, D. Y. Sun, H. J. Xiang, and X. G. Gong. Size-dependent melting behavior of iron nanoparticles by replica exchange molecular dynamics. *Nanoscale*, 4:6307–6311, 2012. doi:10.1039/C2NR30853C.

[54] G. Smith. Phase behavior of some condensed polycyclic aromatics. *Molecular Crystals and Liquid Crystals*, 64(1):15–17, 1980. doi:10.1080/01406568008072649.

[55] H. Takeuchi. Novel method for geometry optimization of molecular clusters: Application to benzene clusters. *Journal of Chemical Information and Modeling*, 47(1):104–109, 2007. doi:10.1021/ci600336p.

[56] K. T. Tang and J. P. Toennies. An improved simple model for the van der waals potential based on universal damping functions for the dispersion coefficients. *The Journal of Chemical Physics*, 80(8):3726–3741, 1984. doi:10.1063/1.447150.

[57] T. S. Totton, D. Chakrabarti, A. J. Misquitta, D. J. Wales, and M. Kraft. Modelling the internal structure of nascent soot particles. *Combustion and Flame*, 157(5):909–914, 2010. doi:10.1016/j.combustflame.2009.11.013.

[58] T. S. Totton, A. J. Misquitta, and M. Kraft. A first principles development of a general anisotropic potential for polycyclic aromatic hydrocarbons. *Journal of Chemical Theory and Computation*, 6(3):683–695, 2010. doi:10.1021/ct9004883.

[59] T. S. Totton, A. J. Misquitta, and M. Kraft. A transferable electrostatic model for intermolecular interactions between polycyclic aromatic hydrocarbons. *Chemical Physics Letters*, 510(1-3):154–160, 2011. doi:10.1016/j.cplett.2011.05.021.

[60] T. S. Totton, A. J. Misquitta, and M. Kraft. Assessing the PAHAP potential with application to the exfoliation energy of graphite. *The Journal of Physical Chemistry A*, 115(46):1368413693, 2011. doi:10.1021/jp208088s.

[61] T. S. Totton, R. Shirley, and M. Kraft. First-principles thermochemistry for the combustion of $TiCl_4$ in a methane flame. *Proceedings of the Combustion Institute*, 33(1):493–500, 2011. doi:10.1016/j.proci.2010.05.011.

[62] T. S. Totton, A. J. Misquitta, and M. Kraft. A quantitative study of the clustering of polycyclic aromatic hydrocarbons at high temperatures. *Physical Chemistry Chemical Physics*, 14:4081–4094, 2012. doi:10.1039/C2CP23008A.

[63] B. W. van de Waal. Significance of calculated cluster conformations of benzene: comment on a publication by D. E. Williams. *Acta Crystallographica*, A37(5):762–764, 1981. doi:10.1107/S0567739481001654.

[64] B. W. van de Waal. Calculated ground-state structures of 13-molecule clusters of carbon dioxide, methane, benzene, cyclohexane, and napthalene. *Journal of Chemical Physics*, 79(8):3948–3961, 1983. doi:10.1063/1.446263.

[65] D. Van Der Spoel, E. Lindahl, B. Hess, G. Groenhof, A. E. Mark, and H. J. C. Berendsen. Gromacs: Fast, flexible, and free. *Journal of Computational Chemistry*, 26(16):1701–1718, 2005. doi:10.1002/jcc.20291.

[66] L. Verlet. Computer "experiments" on classical fluids. I. Thermodynamical properties of Lennard-Jones molecules. *Physical Review*, 159(1):98, 1967. doi:10.1103/PhysRev.159.98.

[67] A. Violi. Modeling of soot particle inception in aromatic and aliphatic premixed flames. *Combustion and Flame*, 139:279–287, 2004. doi:10.1016/j.combustflame.2004.08.013.

[68] H. Wang. Formation of nascent soot and other condensed-phase materials in flames. *Proceedings of the Combustion Institute*, 33(1):41–67, 2011. doi:10.1016/j.proci.2010.09.009.

[69] B. Wersborg, J. Howard, and G. Williams. Physical mechanisms in carbon formation in flames. *Symposium (International) on Combustion*, 14(1):929 – 940, 1973. doi:10.1016/S0082-0784(73)80085-2.

[70] D. E. Williams. Calculated energy and conformation of clusters of benzene molecules and their relationship to crystalline benzene. *Acta Crystallographica*, A36(4):715–723, 1980. doi:10.1107/S056773948000143X.

[71] K. Yehliu, R. L. Vander Wal, and A. L. Boehman. Development of an HRTEM image analysis method to quantify carbon nanostructure. *Combustion and Flame*, 158(9):1837–1851, 2011. doi:10.1016/j.combustflame.2011.01.009.

[72] M. R. Zachariah, M. J. Carrier, and E. Blaisten-Barojas. Properties of silicon nanoparticles: A molecular dynamics study. *The Journal of Physical Chemistry*, 100(36):14856–14864, 1996. doi:10.1021/jp953773w.